Journal of Biomedical Optics

BiomedicalOptics.SPIEDigitalLibrary.org

Spread spectrum time-resolved diffuse optical measurement system for enhanced sensitivity in detecting human brain activity

Kalpesh Mehta
Ali Hasnain
Xiaowei Zhou
Jianwen Luo
Trevor B. Penney
Nanguang Chen

SPIE.

Kalpesh Mehta, Ali Hasnain, Xiaowei Zhou, Jianwen Luo, Trevor B. Penney, Nanguang Chen, "Spread spectrum time-resolved diffuse optical measurement system for enhanced sensitivity in detecting human brain activity," *J. Biomed. Opt.* **22**(4), 045005 (2017), doi: 10.1117/1.JBO.22.4.045005.

Spread spectrum time-resolved diffuse optical measurement system for enhanced sensitivity in detecting human brain activity

Kalpesh Mehta,[a,†] Ali Hasnain,[a,†] Xiaowei Zhou,[a] Jianwen Luo,[b] Trevor B. Penney,[c] and Nanguang Chen[a,*]
[a]National University of Singapore, Department of Biomedical Engineering, Singapore, Singapore
[b]Tsinghua University, School of Medicine, Department of Biomedical Engineering, Beijing, China
[c]National University of Singapore, Department of Psychology, Singapore, Singapore

Abstract. Diffuse optical spectroscopy (DOS) and imaging methods have been widely applied to noninvasive detection of brain activity. We have designed and implemented a low cost, portable, real-time one-channel time-resolved DOS system for neuroscience studies. Phantom experiments were carried out to test the performance of the system. We further conducted preliminary human experiments and demonstrated that enhanced sensitivity in detecting neural activity in the cortex could be achieved by the use of late arriving photons. [DOI: 10.1117/1.JBO.22.4.045005]

Keywords: diffuse optical imaging; functional imaging; spread spectrum.

Paper 160694RR received Oct. 16, 2016; accepted for publication Mar. 15, 2017; published online Apr. 6, 2017.

1 Introduction

Diffuse optical spectroscopy (DOS) and diffuse optical tomography (DOT) can probe hemodynamic changes in large human organs due to the large penetration depth of near-infrared photons in biological tissues.[1,2] Recently, DOS has become increasingly popular in neurosciences as it can provide real-time information about neurovascular coupling in the human brain.[3–5] Moreover, it can be used alone or in combination with other functional imaging modalities, such as electroencephalogram[6–12] and functional magnetic resonance imaging[13–19] to investigate brain function.

While a variety of DOS systems have been reported, most of them fall into three categories: continuous-wave (CW),[20–23] frequency-domain (FD),[23–27] and time-domain (TD) methods.[28–32] Among all the implementations, the CW method is the simplest technique: it is low cost, fast in data acquisition, and portable. The major drawback with this technique is that it measures the combined contributions from photons diffusing through superficial tissues and deep cerebral tissues. The systemic physiological changes in superficial layers (e.g., scalp and skull), due to heart beats and/or blood pressure fluctuation, may vary the intensity of early arriving photons. Such a variation could confound the optical measurements as the early arriving photons usually overwhelm the late arriving photons, which carry information about the deep layers (cortical tissues). As a result, the sensitivity in detecting the signal from the deep layers is limited for the CW method.[33–35] To improve the depth sensitivity, CW domain systems usually resort to multidistance measurements with a number of source-detector pairs.

It has been reported that with a single source-detector pair, a TD system can discriminate between the photons coming from deep regions and those from the superficial layers.[35] Several groups have demonstrated that a TD system provides enhanced sensitivity to cortical hemodynamic changes due to its capability to detect time-resolved arrival of photons. Along with the improvement in depth resolved sensitivity, a time domain system has enhanced localization in detecting hemodynamic changes.[34–36]

In conventional TD DOT systems, an ultrashort pulsed laser is used to illuminate the tissue sample and the optical signal from the sample is detected using either a streak camera[37] or a time correlated single photon counter (TCSPC).[32] The conventional time domain system has several limitations, such as small dynamic range, temporal nonlinearity in the case of streak camera-based detection and long data acquisition time and sensitivity to ambient environment in the case of the TCSPC-based detection. The conventional TD systems are usually bulky, slow, expensive, complicated, and less scalable to increase the number of source detector pairs.[38]

To overcome these issues, a time domain DOT system based on the spread spectrum method was proposed.[39–42] Spread spectrum techniques are used in communication systems for secure and high fidelity communication and have many advantages such as low-error rate, interference rejection, and selective addressing capability. In a spread spectrum method, a communication signal with a particular bandwidth is deliberately spread in the frequency domain to transform it into a wide-band signal. These techniques require the use of pseudorandom number sequences (PRBS) to determine and control the spreading behavior of the signal along the bandwidth. Using this technique, it is possible to use low cost laser diodes as sources and avalanche photodiodes (APDs) as detectors. A variable delay line is combined with an electronic correlator in the detector side to demodulate the optoelectric signal and generate the time resolved profile of arriving photons. Previously, a spread spectrum method-based system was reported for mapping the optical properties of breast tissues.[41]

In this paper, we report a single-channel DOS system for brain functional tests. It is a time-resolved instrument based on our spread-spectrum method. However, new design elements have been included to further reduce the system complexity and

*Address all correspondence to: Nanguang Chen, E-mail: biecng@nus.edu.sg

†These authors contributed equally.

system cost (<$5000). We further demonstrate that such a low-cost system can provide the high performance needed for *in vivo* monitoring of human brain activity.

2 Materials and Methods

2.1 *System Design*

A previously reported spread-spectrum DOT system used a commercially available PRBS generator to generate the spread-spectrum signals.[42] However, commercial PRBS devices are usually bulky and expensive (>$10,000) as they usually come with additional and unnecessary functions. A key improvement in our design is a field programmable gate array (FPGA)-based dual-channel PRBS generator. An FPGA evaluation board (SP605, Xilinx) is chosen to implement two PRBS generators in the same device. The two generators are structurally identical. Each of them includes a 10-stage linear feedback shift register, which abides by a particular sequence generating polynomial $(X^{10} + X^7 + 1)$. A combinational logic circuit is used to predict the subsequent 20 bits within one internal clock cycle (internal clock frequency: 125 MHz). These bits are serialized by the on-board serializer/deserializer (ser/des) to the I/O transceiver port. The serial output is a 2.5 Gbps PRBS (pattern 10) that repeats itself for every $2^{10} - 1$ bits. The output can be seeded with different initial states to form two independent generators, so that their corresponding output sequences are identical but time shifted by an integer multiplication of 400 ps. The minimum delay step size is 400 ps that is limited by the clock rate of FPGA board (2.5 GHz). The dual-channel PRBS generator eliminates the need for a programmable delay line, which costs another few thousand dollars.

As shown in the system schematic (Fig. 1), the dual-channel PRBS generator is controlled by a National Instruments data acquisition (NI-DAQ) device for variable time delay. One of the output PRBS sequences is modulated by a 2-kHz square wave, which functions as the secondary modulation signal. Previously, we used an external Mach–Zehnder modulator to achieve modulated illumination. However, such a fiber-based external modulator is subject to the photorefractive effect, not to mention its high cost (around $6000). In this design, we chose an 850-nm high-speed vertical cavity surface emitting laser (VCSEL) diode

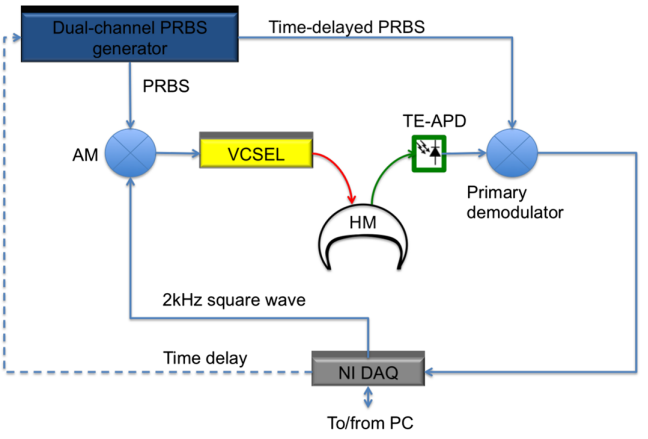

Fig. 1 Schematic of single-channel time-resolved DOS system. AM, analog modulator; HM, head mount; PRBS, pseudorandom bit sequence; TE-APD, thermoelectrically cooled APD; VCSEL, vertical cavity surface emitting laser diode; NI DAQ, National instruments data acquisition device.

(VIXAR Inc, MULTM-000-B002) as the light source, which could be direct intensity modulated with the modulation signal. The VCSEL is fiber coupled to a head mount for brain activity monitoring. A light guide (Edmund optics, 39-366) is also placed on the head mount with a fixed distance from the source fiber. It collects the diffuse reflectance from the brain or a tissue phantom. The collected light is coupled into a thermoelectrically cooled avalanche photodiode (TE-APD, based on Hamamatsu S2383), which converts the weak optical signal into an electrical signal. The optoelectrical signal is preamplified by low-noise amplifiers (not shown in Fig. 1) before demodulation. The first stage demodulation is done by mixing the preamplified optoelectrical signal with the time-delayed PRBS sequence. The down-converted signal is the time-resolved (for a specific time delay) diffuse light intensity carried by the 2 kHz square wave. It is digitized by the NI-DAQ device so that the second-stage demodulation can be carried out numerically on a PC. The sampling rate for the signal acquisition is 50 kS/s. The integration time to record the raw signal for one specific time delay is set to 25 ms. A LABVIEW program on the PC is responsible for scanning the delay time, collecting the raw data, performing secondary demodulation, and recording the time-resolved diffuse light intensity, the so-called temporal point spread function (TPSF).

2.2 *Tissue Phantom and In-Vivo Imaging*

To characterize the performance of the system, a homogeneous tissue phantom was made by diluting 20% Intralipid in a water tank. The diluted solution was 1% in concentration. The true value of reduced scattering coefficient (μ_s') at this concentration was around 8.9 cm^{-1}. Ink solution was added into the diluted Intralipid solution to control its absorption coefficient (μ_a) values. A spectrometer (Ocean Optics, USB4000-VIS-NIR) was used to quantify the true value of the absorption coefficient (μ_a) for various ink concentrations. For homogeneous phantom experiments, three concentrations of ink were used (0.01, 0.02, and 0.03 ml/l). The respective values of absorption coefficient for these concentrations were: 0.08, 0.15, and 0.31 cm^{-1}. A Mie calculator was used to estimate the theoretical value of the reduced scattering coefficient of the Intralipid solution. The system was first tested for its accuracy in quantifying the absorption and scattering coefficients of the homogeneous sample with a source-detector distance of 2.5 cm. A background optical property fitting method[41] was used to simultaneously estimate absorption and scattering coefficients of the homogeneous phantoms.

Compared with continuous wave and frequency domain systems, a conventional time domain system provides enhanced sensitivity to inhomogeneties located at deeper regions using late arriving photons. To demonstrate that our low-cost system can provide similar sensitivity enhancement, it was characterized with experiments in which an absorbing target was embedded in a homogeneous Intralipid solution ($\mu_a = 0.08$ cm^{-1} and $\mu_s' = 8.9$ cm^{-1}). In these experiments, the source and the detector were kept at a distance of 2.5 cm. The source fiber and the detection light guide gently touched the surface of the solution. The absorbing target was a cylindrical tube with a high absorption coefficient of around 0.64 cm^{-1} and a reduced scattering coefficient identical to that of the background medium. It was embedded in the tissue phantom with its center located at different depths (1 to 2.5 cm) but equally distant from both the source and the detector. The tube was 0.5 cm in diameter and 0.5 cm in length. To quantify the contrast enhancement, the perturbation as a function of time of flight was defined as

$$\text{Perturbation}\,(\text{depth, time of flight}) = 100 \times \frac{\text{TPSF}_{\text{inhomo}}(\text{depth, time of flight}) - \text{TPSF}_{\text{homo}}(\text{time of flight})}{\text{TPSF}_{\text{homo}}(\text{time of flight})}, \quad (1)$$

where $\text{TPSF}_{\text{inhomo}}(\text{depth, time of flight})$ and $\text{TPSF}_{\text{homo}}(\text{time of flight})$ were temporal profiles of diffuse photons measured with and without the embedded target, respectively.

In addition to the phantom experiments, we conducted a cognitive experiment on a healthy human subject to demonstrate applicability of our approach to brain functional studies. The research protocol was approved by the National University of Singapore Institutional Review Board. The experiment was designed to record the hemodynamic changes in the middle frontal cortex about 3.5 cm above the left pupil while the participant solved simple arithmetic problems in a short preset duration. A computer program was used to generate random four digit subtraction problems, e.g., "7654 − 3976 = ?." Each cognitive test run was divided into 10 blocks. Each block was 3 min in total, consisting of 1 min of rest + 1 min of problem solving + 1 min of rest. The subject was instructed to solve as many problems as he could in 1 min. A timer was set in the background and the computer screen became blank with a white spot when 1 min of problem solving was over. A healthy right-handed male subject in his twenties was recruited for this experiment. The recorded raw data were averaged over blocks to increase the signal-to-noise ratio.

In the brain measurement experiment, the source-detector distance was 3 cm. The intensities of diffusive photons were measured at 11 time delay points (at a 400-ps interval). The photon intensities averaged over the rest period were considered as base values [$\text{TPSF}_m(\text{time of flight})$]. The changes in optical signal relative to the base values were computed as perturbations.

$$\text{Perturbation}\,(t, \text{time of flight}) = 100 \times \frac{\text{TPSF}_t(\text{time of flight}) - \text{TPSF}_m(\text{time of flight})}{\text{TPSF}_m(\text{time of flight})}. \quad (2)$$

2.3 *Numerical Simulation*

To independently validate our time-resolved measurement results for perturbation quantification, finite element numerical simulations were carried out to theoretically predict the time domain responses. The simulation was based on a coefficient form partial differential equation

$$\frac{n}{c}\frac{\partial \varnothing}{\partial t} + \nabla(-D\nabla\varnothing) + \mu_a\varnothing = P_0(r,t), \quad (3)$$

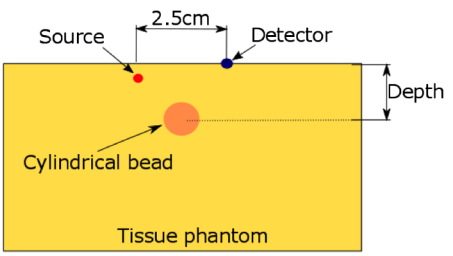

Fig. 2 Two-dimensional cross section of finite element simulation geometry.

where $\varnothing$ is the light fluence rate, D is the diffusion coefficient, μ_a is the absorption coefficient, n is the refractive index, c is the speed of light in vacuum, and $P_0(r,t)$ is the source distribution. The diffusion coefficient is defined as

$$D = \frac{1}{3(\mu_s' + \mu_a)}, \quad (4)$$

where $\mu_s' = (1-g)\mu_s$ is the reduced scattering coefficient. μ_s and g are the scattering coefficient and anisotropy factor of the medium, respectively. A point source with a Gaussian temporal profile [1 ns full width half maximum (FWHM)] was used to excite the sample. The simulation geometrical configuration is shown in Fig. 2. Like the tissue phantom experiment, a source detector pair separated by 2.5 cm were used. The background optical properties used in simulations were identical to those in the phantom experiments ($\mu_a = 0.08$ cm^{-1} and $\mu_s' = 8.9$ cm^{-1}). The point source was located at one mean free path distance ($1/\mu_s'$) inside the medium. A $15 \times 15 \times 15$ cm^3 cube was used to define the tissue phantom geometry. At the bottom and side surfaces, zero rate of change in fluence was used as the boundary condition to simulate a semi-infinite medium. On the top surface (Intralipid air interface) where the source and detector were located, the robin boundary condition was applied.

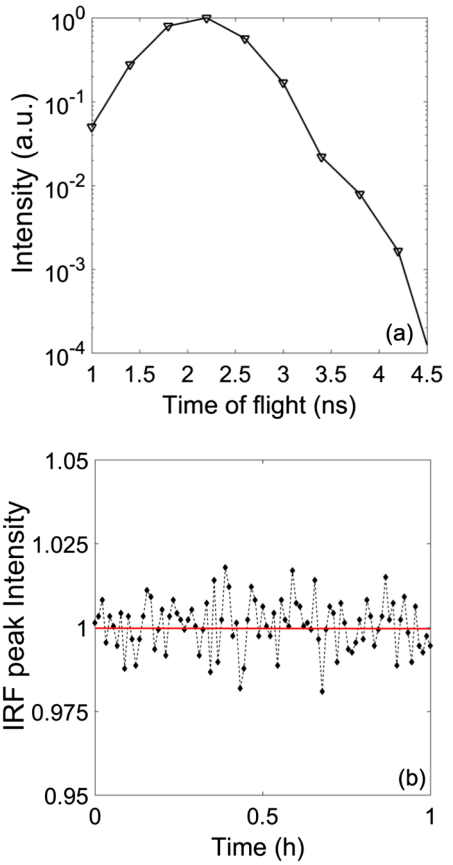

Fig. 3 (a) Measured IRF from a white diffusive reflecting surface; (b) IRF peak value measured over a period of 1 h.

A cylindrical bead was included in the background medium as an inhomogeneity. The bead had a diameter of 0.5 cm and a length of 0.5 cm. The absorption coefficient for the bead was 0.64 cm^{-1} and the reduced scattering coefficient of the bead was the same as that of the background medium. The bead was located at a depth varying from 1 to 2.5 cm.

3 Results and Discussion

To quantify the system stability and the system impulse response function (IRF), a TPSF was measured by placing a white reflecting surface at 30 cm away from the source-detector pair. Figure 3(a) shows an IRF measured from the reflecting surface. The FWHM of the IRF was around 1 ns. The theoretical limit of time resolution should be 400 ps given a PRBS bit rate of 2.5 Gbps. However, various components used in the system limited the overall system bandwidth. For example, the APD detector had a bandwidth of 600 MHz, which was the main bottleneck for a better time resolution. To demonstrate the long-term system stability, we repeated the above-mentioned IRF measurement at intervals of 1 min over a period of 1 h. The fluctuation in the peak value (normalized to the 1-h time average) of the IRF was <1% [Fig. 3(b)].

To evaluate the performance of our system in quantifying the optical properties of a homogeneous medium, the system was tested on homogeneous phantoms with different absorption coefficients (0.08, 0.15, and 0.31 cm^{-1}), but with the same reduced scattering coefficient (8.9 cm^{-1}). Figure 4(a) compares the IRF and TPSF's. The IRF of the system was normalized to its peak value and the TPSF's for different absorption coefficients were normalized to the maximum value of the TPSF measured from the phantom of a low absorption coefficient of 0.08 cm^{-1}. In Fig. 4(b), the true values of the absorption coefficients are compared with the absorption coefficients obtained by fitting the experimental data. The true values of the absorption coefficient were measured using the Ocean Optics spectrometer. Figure 4(c) shows the reduced scattering coefficient values obtained for all three homogeneous tissue phantoms.

The main advantage of time domain diffuse optical measurement is the enhanced sensitivity to deep perturbation in comparison with CW and FD methods. Our experimental results from inhomogeneous phantoms were validated against numerical simulation results. Figure 5(a) shows a simulated TPSF excited by a pulse 1 ns in duration (FWHM). Figure 5(b) shows an experimental TPSF measured from a homogeneous phantom of the same optical properties. The mean value (solid line) and standard deviations (error bars) were estimated from 20 repeated measurements. The TPSF was perturbed once the absorber was embedded in the otherwise homogeneous background. Figure 5(c) shows the perturbation predicted by numerical simulation and Fig. 5(d) shows the experimental perturbation levels for various times of flight of diffusive photons. For both simulations and experiments, the inhomogeneity was placed at various depths in the tissue phantom. The time of flight was mapped from the PRBS delay time after system calibration. Both experimental and simulation results show that, when the absorber was located in the shallow region (1 cm), the perturbation changed at a rather slow rate with an increasing time of flight. In contrast, the rate of change in perturbation increased significantly for late arriving photons when the absorber was moved to a deeper

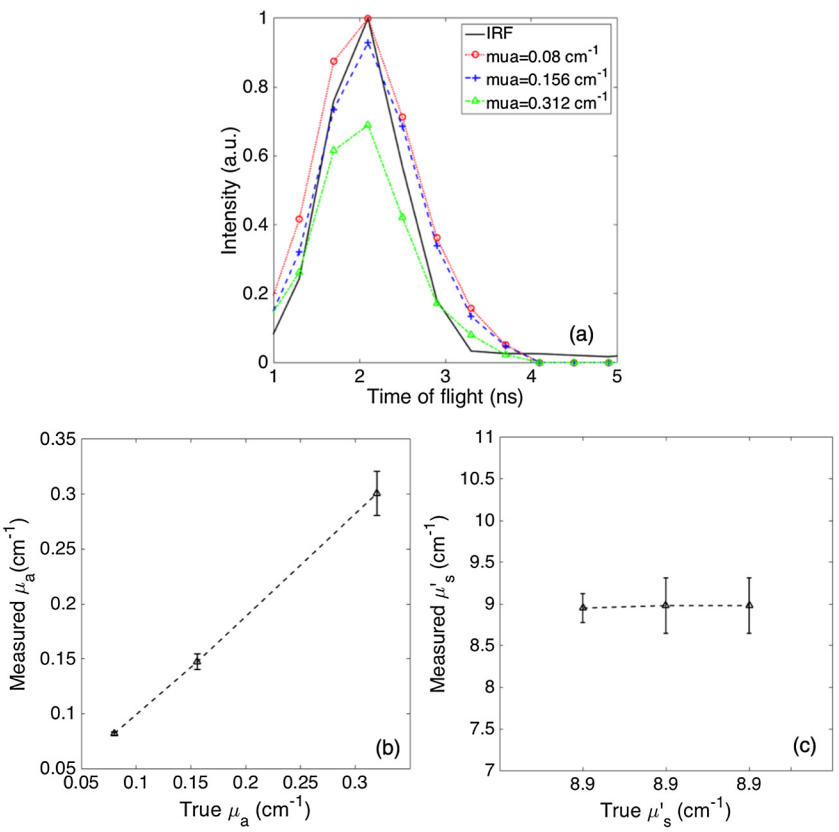

Fig. 4 (a) System IRF and TPSF measured from three phantoms of different absorption coefficients (indicated in legend); (b) comparison between measured and true values of absorption coefficients; and (c) comparison between measured and true values of reduced scattering coefficients.

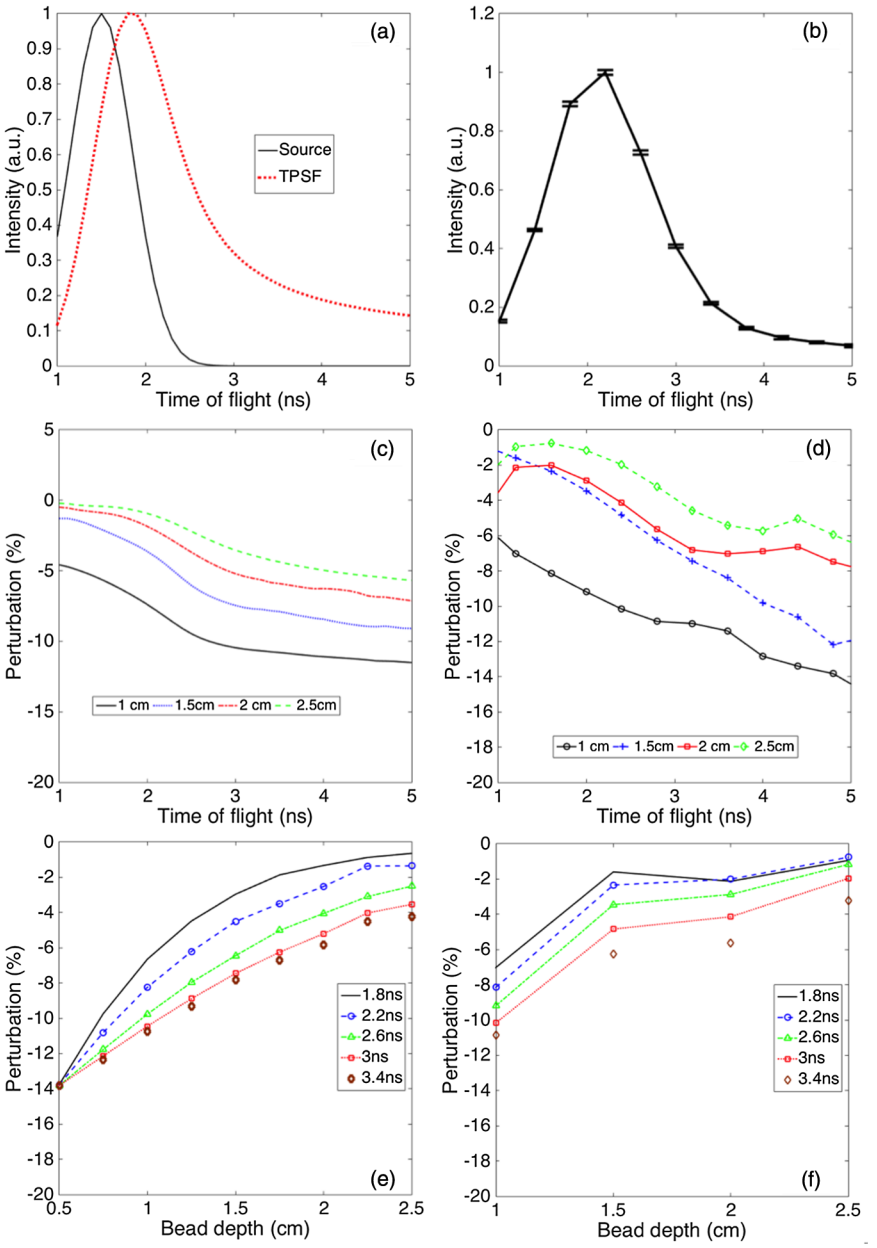

Fig. 5 (a) A normalized TPSF (red) obtained using numerical simulation and an excitation source profile (black); (b) a normalized experimental TPSF obtained from a homogeneous phantom; (c) numerical predicted perturbation as a function of time of flight (legend indicates the bead location); (d) experimentally measured perturbation as a function of time of flight (legend indicates location of bead); (e) numerical predicted perturbation as a function of bead depth (legend indicates different delay gate); and (f) experimentally measured perturbation as a function of bead depth (legend indicates different time of flight).

region (2.5 cm). Shown in Figs. 5(e) and 5(f) are perturbations as functions of bead depth based on simulation and experimental data, respectively. These results clearly demonstrated that late arriving photons captured by our system provided higher perturbation and therefore higher sensitivity when the absorber was located at a deep location. The phantom experimental results serve as direct evidence that our single-channel time resolved DOS system is capable of detecting heterogeneities deep inside a turbid medium with improved sensitivity.

Similarly, the human subject experiment also demonstrated the capability of our system in providing enhanced contrast using the late arriving photons. Figure 6(a) shows the measured TPSF from the human subject during the rest period. The Fig. 6(b) shows the block-averaged time traces of the diffuse light intensities, which reflects the underlying hemodynamic changes in the frontal cortex. Five traces are associated with five different times of flight, i.e., 2 ns (blue dot), 2.4 ns (black dot), 2.8 ns (black asterisk), 3.2 ns (red dot), and 3.6 ns (red asterisk), respectively. It is clear that late arriving photons show high perturbation values compared to the early arriving photons.

To conclude, we have successfully developed a low-cost, single-channel DOS system for brain functional monitoring and studies. We have demonstrated experimentally that this system can provide enhanced sensitivity in detecting human brain activities.

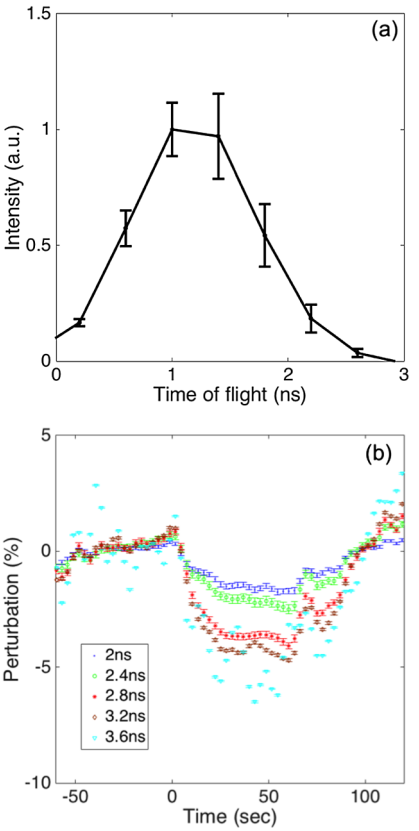

Fig. 6 (a) Measured TPSF (normalized) for a human subject during the rest period; (b) effect of time of flight on optical signals associated with hemodynamic changes. Time zeros corresponds to the onset of the problem solving phase for the cognitive task. Legend indicates the time of flight.

Disclosures

Dr. Chen reports grants from the National Medical Research Council and grants from the National University of Singapore during the conduct of the study. All the other authors have nothing to disclose.

Acknowledgments

This work was supported in part by the National Medical Research Council grants (NMRC/CBRG/0100/2015 and NMRC/CBRG/0036/2013) and internal funding from the National University of Singapore.

References

1. T. Durduran et al., "Diffuse optics for tissue monitoring and tomography," *Rep. Prog. Phys.* **73**, 076701 (2010).
2. A. Yodh and B. Chance, "Spectroscopy and imaging with diffusing light," *Phys. Today* **48**(3), 34–40 (2008).
3. D. A. Benaron et al., "Noninvasive functional imaging of human brain using light," *J. Cereb. Blood Flow Metab.* **20**, 469–477 (2000).
4. A. T. Eggebrecht et al., "Mapping distributed brain function and networks with diffuse optical tomography," *Nat. Photonics* **8**, 448–454 (2014).
5. A. Villringer et al., "Non-invasive optical spectroscopy and imaging of human brain function," *Trends Neurosci.* **20**(10), 435–442 (1997).
6. M. Butti et al., "Multimodal analysis of a sustained attention protocol: continuous performance test assessed with near infrared spectroscopy and EEG," in *Conf. Proc.: Annual Int. Conf. of the IEEE Engineering in Medicine and Biology Society. IEEE Engineering in Medicine and Biology Society. Annual Conf.*, Vol. 1, pp. 1040–1043 (2006).
7. R. J. Cooper et al., "A tissue equivalent phantom for simultaneous near-infrared optical tomography and EEG," *Biomed. Opt. Express* **1**(2), 425–430 (2010).
8. R. J. Cooper et al., "Design and evaluation of a probe for simultaneous EEG and near-infrared imaging of cortical activation," *Phys. Med. Biol.* **54**(7), 2093–2102 (2009).
9. J. W. de Vries, G. H. Visser, and P. F. Bakker, "Neuromonitoring in defibrillation threshold testing. A comparison between EEG, near-infrared spectroscopy and jugular bulb oximetry," *J. Clin. Monitor.* **13**(5), 303–307 (1997).
10. R. P. Kennan et al., "Simultaneous recording of event-related auditory oddball response using transcranial near infrared optical topography and surface EEG," *Neuroimage* **16**(3 Pt 1), 587–592 (2002).
11. S. Telkemeyer et al., "Acoustic processing of temporally modulated sounds in infants: evidence from a combined near-infrared spectroscopy and EEG study," *Front. Psychol.* **1**, 62 (2011).
12. C. Y. Tse et al., "The functional role of the frontal cortex in pre-attentive auditory change detection," *Neuroimage* **83**, 870–879 (2013).
13. B. Frederick, L. D. Nickerson, and Y. Tong, "Physiological denoising of BOLD fMRI data using regressor interpolation at progressive time delays (RIPTiDe) processing of concurrent fMRI and near-infrared spectroscopy (NIRS)," *Neuroimage* **60**(3), 1913–1923 (2012).
14. Y. Tong, K. P. Lindsey, and B. de Frederick, "Partitioning of physiological noise signals in the brain with concurrent near-infrared spectroscopy and fMRI," *J. Cerebral Blood Flow Metab.* **31**(12), 2352–2362 (2011).
15. Y. Tong, P. R. Bergethon, and B. D. Frederick, "An improved method for mapping cerebrovascular reserve using concurrent fMRI and near-infrared spectroscopy with regressor interpolation at progressive time delays (RIPTiDe)," *Neuroimage* **56**(4), 2047–2057 (2011).
16. S. Tak et al., "Quantitative analysis of hemodynamic and metabolic changes in subcortical vascular dementia using simultaneous near-infrared spectroscopy and fMRI measurements," *Neuroimage* **55**(1), 176–184 (2011).
17. Y. Tong and B. D. Frederick, "Time lag dependent multimodal processing of concurrent fMRI and near-infrared spectroscopy (NIRS) data suggests a global circulatory origin for low-frequency oscillation signals in human brain," *Neuroimage* **53**(2), 553–564 (2010).
18. S. Tak et al., "Quantification of CMRO(2) without hypercapnia using simultaneous near-infrared spectroscopy and fMRI measurements," *Phys. Med. Biol.* **55**(11), 3249–3269 (2010).
19. J. Lee et al., "Origins of spatial working memory deficits in schizophrenia: an event-related FMRI and near-infrared spectroscopy study," *PLoS One* **3**(3), e1760 (2008).
20. Y. C. Lin et al., "Continuous wave spectroscopy with diffusion theory for quantification of optical properties: comparison between multi-distance and multi-wavelength data fitting methods," *Adv. Exp. Med. Biol.* **923**, 337–343 (2016).
21. A. Wang, R. Lu, and L. Xie, "Finite element modeling of light propagation in turbid media under illumination of a continuous-wave beam," *Appl. Opt.* **55**(1), 95–103 (2016).
22. S. Okawa et al., "Reconstruction of localized fluorescent target from multi-view continuous-wave surface images of small animal with lp sparsity regularization," *Biomed. Opt. Express* **5**(6), 1839–1860 (2014).
23. J. P. Culver et al., "Three-dimensional diffuse optical tomography in the parallel plane transmission geometry: evaluation of a hybrid frequency domain/continuous wave clinical system for breast imaging," *Med. Phys.* **30**(2), 235–247 (2003).
24. H. Zhao et al., "Near-infrared frequency domain system and fast inverse Monte Carlo algorithm for endoscopic measurement of tubular tissue," *J. X-ray Sci. Technol.* **19**(1), 57–68 (2011).
25. K. S. No et al., "Design and testing of a miniature broadband frequency domain photon migration instrument," *J. Biomed. Opt.* **13**(5), 050509 (2008).
26. N. G. Chen et al., "Simultaneous near-infrared diffusive light and ultrasound imaging," *Appl. Opt.* **40**(34), 6367–6380 (2001).
27. N. G. Chen et al., "Portable near-infrared diffusive light imager for breast cancer detection," *J. Biomed. Opt.* **9**(3), 504–510 (2004).
28. P. Taroni et al., "Breast tissue composition and its dependence on demographic risk factors for breast cancer: non-invasive assessment by time

domain diffuse optical spectroscopy," *PLoS One* **10**(6), e0128941 (2015).
29. I. Bargigia et al., "Time-resolved diffuse optical spectroscopy up to 1700 nm by means of a time-gated InGaAs/InP single-photon avalanche diode," *Appl. Spectrosc.* **66**(8), 944–950 (2012).
30. A. Puszka et al., "Time-resolved diffuse optical tomography using fast-gated single-photon avalanche diodes," *Biomed. Opt. Express* **4**(8), 1351–1365 (2013).
31. F. Gao, H. Zhao, and Y. Yamada, "Improvement of image quality in diffuse optical tomography by use of full time-resolved data," *Appl. Opt.* **41**(4), 778–791 (2002).
32. R. J. Cooper et al., "MONSTIR II: a 32-channel, multispectral, time-resolved optical tomography system for neonatal brain imaging," *Rev. Sci. Instrum.* **85**(5), 053105 (2014).
33. E. Kirilina et al., "The physiological origin of task-evoked systemic artefacts in functional near infrared spectroscopy," *Neuroimage* **61**, 70–81 (2012).
34. J. Selb et al., "Improved sensitivity to cerebral hemodynamics during brain activation with a time-gated optical system: analytical model and experimental validation," *J. Biomed. Opt.* **10**(1), 011013 (2005).
35. L. Zucchelli et al., "Method for the discrimination of superficial and deep absorption variations by time domain fNIRS," *Biomed. Opt. Express* **4**, 2893–2910 (2013).
36. J. Selb, A. M. Dale, and D. A. Boas, "Linear 3D reconstruction of time-domain diffuse optical imaging differential data: improved depth localization and lateral resolution," *Opt Express* **15**(25), 16400–16412 (2007).
37. C. V. Zint et al., "Streak camera: a multidetector for diffuse optical tomography," *Appl. Opt.* **42**(16), 3313–3320 (2003).
38. A. Torricelli et al., "Time domain functional NIRS imaging for human brain mapping," *Neuroimage* **85**(Pt 1), 28–50 (2014).
39. N. Chen and Q. Zhu, "Time-resolved diffusive optical imaging using pseudo-random bit sequences," *Opt. Express* **11**(25), 3445–3454 (2003).
40. N. G. Chen and Q. Zhu, "Time-resolved optical measurements with spread spectrum excitation," *Opt. Lett.* **27**(20), 1806–1808 (2002).
41. W. Mo et al., "Quantitative characterization of optical and physiological parameters in normal breasts using time-resolved spectroscopy: in vivo results of 19 Singapore women," *J. Biomed. Opt.* **14**(6), 064004 (2008).
42. W. Mo and N. Chen, "Fast time-domain diffuse optical tomography using pseudorandom bit sequences," *Opt. Express* **16**(18), 13643–13650 (2008).

Nanguang Chen received his BEng degree in electrical engineering from Hunan University in 1988, his MSc degree in physics from Peking University in 1994, and his PhD in biomedical engineering from Tsinghua University in 2000. Currently, he is an associate professor in the Department of Biomedical Engineering, the National University of Singapore. His research interests cover mainly biomedical optics and optical imaging.

Biographies for the other authors are not available.